Journal of Additive Manufacturing Technologies
DOI: 10.18416/JAMTECH. 2111604

Infinite Science | Publishing

3D Thermal Modelling and Simulation of Ti–6Al–4V alloy Processed by Selective Laser Melting

Demiray M. A.[1], **Sekerci B.**[2], **Kayacan M. C.** [1*], **Baykasoğlu C.**[3]

[1] *Department of Mechanical Engineering, Suleyman Demirel University, Isparta, Turkey*
[2] *YETEM , Suleyman Demirel University, Isparta, Turkey*
[3] *Department of Mechanical Engineering, Hitit University, Çorum, Turkey*
[*] *Corresponding author, email: cengizkayacan@sdu.edu.tr*

Abstract

Selective laser melting (SLM) is the most widely used metal additive manufacturing (AM) technique due to its ability to manufacture complex-shaped parts with the desired tolerances. In the present study, a three-dimensional finite element (FE) heat transfer model for the SLM process was developed and multi-track simulations were conducted to predict maximum temperatures and melt pool dimensions depends on the process parameters such as laser power, scanning speed and hatching distance for Ti6Al4V powder. FE simulations for different process parameters were conducted in ABAQUS as it provides a parametric job possibility within its Fortran subroutines. Goldak volumetric laser heat source model was used as the flux source and material properties were revealed as temperature-dependent. During laser scanning, it was observed that powder material is melted by heat source through at least one layer and this leads to interlayer connection as expected. Besides, maximum temperatures were found stable from the beginning to the end of the track until it achieves an equilibrium regime in view of temperature distribution. The fidelty of the simulation was revealed by comparing melt pool dimensions and maximum temperatures with both experimental and simulation studies in the literature. Furthermore, the melt pool depth to width ratios were examined comparing to the literature. Maximum track temperatures rises from 1st track to the last 4th track as in 2550-3250 ^{0}C. On the other hand, selected process parameters were pointed out as suitable to fuse laser tracks effectively with its smaller D/W ratio than 0.5 which is possible keyhole limit.

Keywords: Heat transfer modeling, Process simulation, Selective laser melting.

1. Introduction

Additive manufacturing (AM) and specifically selective laser melting (SLM) method have become a common manufacturing method in parallel to the 4th digital revolution all over the world. SLM has serious advantages such as manufacturing ability for complex geometries without a cutting tool, using the possibility of improved computer and laser technology, less material cost, lattice structure manufacturing skills, etc. [1,2]. Although these advantages, control of the big temperature gradients, part distortions during manufacturing process sourced by heating-cooling cycles, residual stresses, keyhole case, balling effect and porosity issues bring the optimization of process parameters problem and this makes the SLM still a complex method [3-5].

In recent years, several studies have been conducted to examine and minimize the mentioned problematic issues in the SLM process. At this point, the most common approaches used in solving these problems are substrate preheating and remelting [6-8], developing scanning strategies [9-10] and experimental trials to optimize the effects of the process parameters [11-13]. Trial and error-based experimental studies to prevent or minimize the aforementioned problems can take the literature to the next step but are still time-consuming and costly [14].

In parallel to improving computer skills, modeling and simulation of the whole SLM process have become very popular in the last 20 years to predict the magnitude of heat transfer and its effects on other properties. Williams and Deckard [15] described one dimensional (1D) simulation model to investigate the effects of process parameters on density and mechanical properties of polycarbonate. Next studies continued with laser process simulations for two-dimensional (2D) and three-dimensional (3D) problems [16,9]. In another study, Ibraheem et al. [17] conducted a 3D simulation study by using the new “Element Birth and Death” method in ANSYS. The model was designed in 20x20x9 mm and they assumed that there is no latent heat effect because of small melt pools. Roberts et al. [18] conducted a simulation of SLM by using the same method to compare simulation results with Fisher’s experimental data[19]. The study was covered by a 4-layer ANSYS simulation with each of has 5 reciprocating laser tracks with Gaussian flux distribution. For modeling, conductivity, density and specific heat temperature-dependent values were used from the literature. Optimum process parameters belong to EOS

M250ex were used to predict the temperature of 1x1x0.15 mm powder bed and 3x3x3 mm substrate in Ref. [19]. Besides, Li et al. [20] developed a 3D FE model with a 3x1.8x0.4 mm substrate and 2.2x1.1x0.1 mm powder layer. Temperature-dependent material properties were taken from the ANSYS library. Powder bed porosity was set to 0.5 and %35 absorptivity value used in Ref. [20]. Fu and Guo [21] used Gaussian surface heat flux as a heat source and simulated temperature gradients in 4x1x0.5 mm substrate and 2x0.2x0.15 mm powder layer by using 1x10x5 micron elements in ABAQUS. They wrote a DFLUX user subroutine to move the heat source onto 5 powder layers. Temperature-dependent material properties were taken from the literature for Ti-6Al-4V alloy. Several studies also used Goldak volumetric heat source and similar material properties [22, 23]. A brief literature review on the FE process simulation of SLM for different materials can be found in Refs. [24-26] .

This study focused on the FE thermal modeling of the SLM process for Ti-6Al-4V. Altough there are many thermal modelling study in the literature, most of the studies are not compherensive and effect of process parameters and related simulating datas still have blanks for this area. In this study, process model is developed using commercial software ABAQUS since it has advantages and multifunctionality by its Phyton-based coding algorithm and Fortran-based subroutines to set process parameters easily [27,28]. To obtain more accurate temperature distribution and melt pool dimensions, a detailed process model was developed firstly. Then, detailed temperature-dependent material properties and heat transfer coefficient were calculated and defined in the model. Temperature variations with their peak values were revealed for different laser power, speed and hatch distances. Finally, melt pool dimensions calculated to investigate both depth to width ($\frac{D}{W}$) ratios and overlap depths to understand how melt pool dimensions change for a set of effective process parameters in a certain interval.

2. Material and methods

In this section, FE thermal process model and its components (e.g., governing equations, heat source model, material properties, model domain, mesh and boundary conditions) were discussed in detail.

2.1. Governing Equations and Goldak Double Ellipsoidal Heat Source Model

In SLM, there is a transient thermal moving heat source problem exists. In the beginning, the first law of thermodynamics in view of heat flux balance can lead to the solution. Due to the powder bed can assume as a uniform distributed control volume, laser heat flux is absorbed by the powder bed and it causes an enthalpy change. On the other hand, it diffuses by conduction, convection and radiation to the environment fluid (Argon for Ti-6Al-4V). Additionally, the phase change and latent heat effect should be also considered. Powder bed also can be modeled as continuous and homogeny media. Thus, the governing equation can be written as [18,29,30];

$$\rho(\mathrm{T}).\mathrm{C_p}(\mathrm{T}).\frac{\partial \mathrm{T}}{\partial \mathrm{t}} = \mathrm{k}(\mathrm{T}).\left(\frac{\partial^2 \mathrm{T}}{\mathrm{x}^2} + \frac{\partial^2 \mathrm{T}}{\mathrm{y}^2} + \frac{\partial^2 \mathrm{T}}{\mathrm{z}^2}\right) + \mathrm{q_{la}} + \mathrm{q_{rad}} + \mathrm{q_{conv}} \tag{1}$$

where, ρ is density, C_p is the specific heat at constant pressure, k is thermal conductivity and derivative terms represent the Fourier 3-D conduction. While the right-hand side contains heat flux that diffuses by conduction, convection, radiation and related laser moving heat source respectively, left-hand side represents stored energy or enthalpy change in powder layer. For the heat source $\mathrm{q_{la}}$, a point-related volumetric heat source called Goldak volumetric double ellipsoidal heat source described firstly by Goldak et al. [31] can be used. According to this model, moving heat source combines different front and rear parts of the heat dispersions and there is a Gaussian distribution. The literature revealed that the Goldak model is more adaptable for high energy density values [23]. The Goldak double ellipsoidal model can be defined as [31];

$$\begin{cases} \dot{\mathrm{Q}}_{\mathrm{f(x,y,z)}} = \frac{6.\sqrt{3}.\mathrm{f_f}.\eta_{\mathrm{abs}}.\mathrm{P}}{\pi.\sqrt{\pi}.\mathrm{a_f}.\mathrm{b}.\mathrm{c}}\mathrm{e}^{-\left(\frac{3\mathrm{x}^2}{\mathrm{a_f}^2}+\frac{3\mathrm{y}^2}{\mathrm{b}^2}+\frac{3\mathrm{z}^2}{\mathrm{c}^2}\right)} \\ \dot{\mathrm{Q}}_{\mathrm{r(x,y,z)}} = \frac{6.\sqrt{3}.\mathrm{f_r}.\eta_{\mathrm{abs}}.\mathrm{P}}{\pi.\sqrt{\pi}.\mathrm{a_r}.\mathrm{b}.\mathrm{c}}\mathrm{e}^{-\left(\frac{3\mathrm{x}^2}{\mathrm{a_r}^2}+\frac{3\mathrm{y}^2}{\mathrm{b}^2}+\frac{3\mathrm{z}^2}{\mathrm{c}^2}\right)} \end{cases} \tag{2}$$

In Eq. 2, P is laser power, η_{abs} is material absorbtivity, $\mathrm{f_f}$ and $\mathrm{f_r}$ are respectively front and rear portion of heat fractions which dispersed over the ellipse, a, b and c are double ellipsoidal semi-axial dimensions along x-, y- and z- coordinates. Gaussian double ellipsoidal volumetric heat source was shown in Fig. 1 with elliptic parameters [32]. To apply Goldak volumetric model, a, b and c parameters must be adjusted. Since there is not enough experimental data, $\mathrm{a_f}$ and b parameters were set to equal half of laser spot diameter as 40 µm[33]. For c parameter, it was revealed that the maximum penetration depth is 65 µm for Ti6Al4V material [34]. Hence, c was selected as 65 µm. In order to calculate $\mathrm{a_f}$ value, the approximation below was used [31];

$$\frac{\mathrm{f_f}}{\mathrm{f_r}} = \frac{\mathrm{a_f}}{\mathrm{a_r}} \tag{3}$$

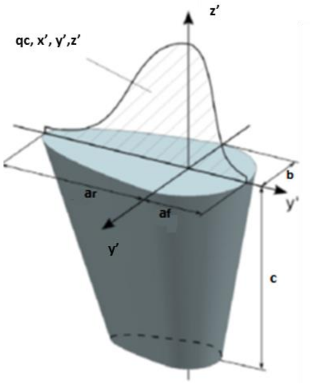

Fig 1. Goldak Double Ellipsoidal Heat Source Parameters [32].

Besides, other assumptions were also made in the modeling. At this point, convection and radiation were applied on the top surface of the powder bed, and other surfaces were fixed at room temperature. Besides, volume shrinkage was also neglected [35,36].

2.2. Material Properties

To create an accurate thermal model for SLM process, material properties found out as temperature-dependent. Solid Ti-6Al-4V properties for density, conductivity and specific heat from room temperature to melting point directly acquired from experimental data [38]. To calculate powder density, a mushy zone between solidus and liquidous temperatures is taken into account by Eqs. 4 and 5 [30];

$$\rho_{po}(T) = \rho_{fl}(T)\phi + (1-\phi)\,\rho_{so}(T) \tag{4}$$

$$\rho_{po} = \begin{cases} \rho_{po}(T)\ ,\ \ T_0 \le T \le T_s \\ \frac{\rho_{so}(T_l)po(T_s)-\rho_{fl}(T_s)}{(T_l-T_s)}.(T-T_s)\ +\rho_{po}(T_s)+\rho_{fl}(T_s)\ ,\ T_s < T < T_l \\ \rho_{so}\ ,\ \ T \ge T_l \end{cases} \tag{5}$$

In Eqs. 4 and 5, ρ is density and ϕ is the porosity of powder bed. Sub-indices po, so and *fl* represent the powder, solid, fluid properties, respectively. Besides, *l* and *s* denote solidus and liquidous temperatures, respectively. The porosity was taken between 0.3-0.4 the most of the studies in the literature [*29,35,38,39*]. Similarly, porosity was chosen as 0.3 in this study.

During the liquid to solid pase changing process, there will be emitted an extra energy which called latent heat and raise specific heat to the higher values. To consider phase change, Eqs. 6-8 applied which has also latent heat effect to obtain specific heat during also phase changing [40,41];

$$C_{po} = ((1-\phi)\rho_{so}C_{so} + \phi.\rho_{fl}C_{fl})/\rho_{po} \tag{6}$$

$$\left\{cp_{po} = \begin{cases} cp_{po}(T)\ ,\ \ T_0 \le T \le T_s \\ (\frac{cp_{so}(T_l)-cp_{po}(T_s))}{(T_l-T_s)}.(T-T_s)\ +cp_{po}(T_s)\ ,\ \ T_s < T < T_l \\ cp_{so}\ ,\ \ T \ge T_l \end{cases}\right. \tag{7}$$

$$c = c_s + \frac{L_f(\{T-T_s)\}}{\Delta T_f^2} + \frac{L_v(\{T-T_l)\}}{\Delta T_v^2} \tag{8}$$

where c is the specific heat; L_f and L_v are fusion and vaporization latent heats; ΔT_f and ΔT_v are fusion and vaporization temperatures differences, respectively.

Similar to specific heat and density calculations, the mushy zone was also taken into account by Eq. 11 to obtain powder conductivity values based on Eqs. 9 and 10[36];

$$\frac{K_{po}}{K_{fl}} = 1-\sqrt{1-\varphi}\left(1+\varphi.\frac{K_r}{K_{fl}}\right)+\sqrt{1-\varphi}.\left(\frac{2}{1-\frac{K_f}{K_{so}}}\right).\left(\frac{1}{1-\frac{K_{fl}}{K_{so}}}\right).\left(1-\frac{K_{fl}}{K_{so}}\right).\ln\left(\frac{K_{so}}{K_{fl}}\right)+\left(\frac{K_r}{K_{fl}}\right) \tag{9}$$

$$K_r = 4.F.\sigma.\left(T_p\right)^3.D_p \tag{10}$$

$$k_{eff} = \left\{\begin{cases} k_{po}\ ,\ \ T_0 \le T \le T_s \\ ((k_{so}(T_l)-k_{po}(T_s))/(T_l-T_s))\ +k_{po}(T_s),\ \ \ T_s < T < T_l \\ k_{so}\ \ ,\ T \ge T_l \end{cases}\right. \tag{11}$$

where K_r is a constant which is for micro radiation effects, F is an experimental constant, D_p is average powder diameter. Fluid density is calculated for Argon as temperature-dependent, fluid specific heat used its constant value between 0 to 2000 °C for Argon, and powder bed conductivity was calculated as temperature-dependent. All calculated material properties were showed in Fig. 2 as graphical representations.

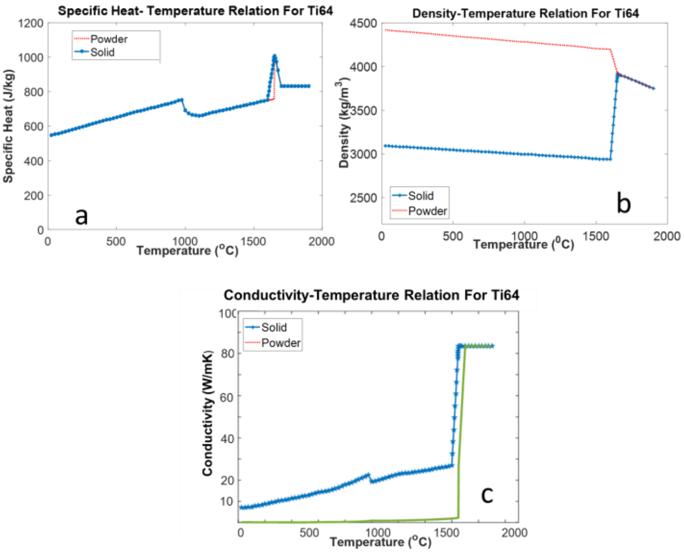

Fig 2. Solid and Powder Material Properties for Ti-6Al-4V a) Specific Heat, b) Density and c) Conductivity.

Both natural and forced convective terms were considered in literature [34,38]. We assumed the natural one is acceptable since EOS Model M280 SLM machine contains an inert gas input mouth about 10 cm above the powder bed. Thus, convection type can be assumed as natural convection due to the distance between gas flow and powder bed top surface in view of the model dimensions. To apply natural convection and find out convection coefficient, definitions in Eq. 12 and the solution formula in Eq. 13 can be used;

$$h_c = \frac{Nuk_f}{L},\quad Gr = \frac{g\left(L^3\rho_f^2\beta_f(T-T_{inf})\right)}{\eta_f^2},\quad Pr = \frac{\eta_f C_f}{k_f} \tag{12}$$

$$\sqrt{Nu} = \sqrt{Nu_0} + \left(\frac{\frac{GrPr}{300}}{\left(1+\left(\frac{0.5}{Pr}\right)^{\frac{9}{16}}\right)^{\frac{16}{9}}}\right)^{\frac{1}{6}},\ \ L = \frac{\text{Surface area}}{\text{Perimeter}} \tag{13}$$

By using Eq. 12 and 13, average h_c=20 W/ m^2K value calculated by using EES (Engineering Equation Solver). For the radiative term, the emissivity value is also a critical parameter. Some researchers have revealed the temperature-dependent emissivity values for Ti-6Al-4V [29,41]. Most of the studies were used emissivity as a constant among 0.4-0.7 [38,41]. It is known that powder emissivity has higher values than solid emissivity. Hence, in this study, the emissivity value was chosen as 0.7 for Ti-6Al-4V [41].

2.3. Computational Domain, FE Model Parameters and Boundary Conditions

ABAQUS adopts an implicit backward difference scheme to calculate nodal temperatures within Newton Raphson iterative method. Consistent with the proposed method, DC3D8 8 node brick element was employed in the 3D model. To determine optimum element size, a mesh convergence test was conducted from 40x40x10 µm to 5x5x10 µm with ½ ratio increments. Finally, element dimensions were determined as 10x10x10 µm^3 to conduct an efficient analysis. Fig. 3a shows the result of different meshes at 170 W power, 1.25 m/s speed and 100 µm hatch, and Fig 3b reveals the element number throughout the beam area.

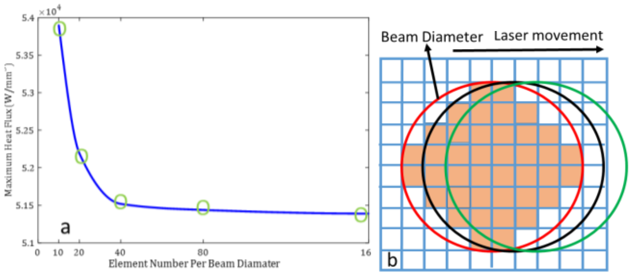

Fig 3. a) Maximum Heat Flux Versus Element Number Per Beam Diameter For The Center Point of The First Track and b) Element Distribution Per Laser Beam

The computational domain was determined as 0.9x0.9x0.4 mm^3 for substrate and 0.7x0.7x0.03 mm^3 for the powder bed. 100 µm of offset value was defined from the edges in direction of x- and y- coordinates to avoid negative edge heat accumulation effects and to prevent heat transfer to the space at half of the edges. Fig. 4 shows the FE simulation model for deposition with three layers.

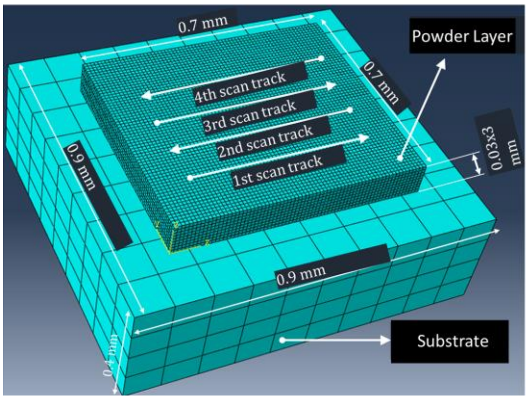

Fig. 4. 3D Simulation Model

In this study, three different power, speed and hatch values used in simulations. Other parameters were kept constant. Table 1 shows the used parameters.

Table 1. Simulation and process parameters.

Laser Power (W)	150–170 - 190	Solidus and Liquidous (℃)	1600, 1650,
Scaning Speed (m/s)	1-1.25 - 1.5	Vaporization (℃)	2860
Hatching Distance (mm)	0.08 - 0.1 - 0.12	Latent Heat Of Fusion and Vapor (J/kg)	295000, 9860000
Beam Diam. (mm)	0.08	Porosity (%)	30
Layer Thick.(mm)	0.03	Absorptivity (%)	70
Powder Material	Ti6Al4V	Emissivity (%)	70

Selecting a suitable time step is also crucial to get accurate temperature results. For this goal, step time calculated with the following equation [42];

$$\min \Delta t = \frac{\Delta x}{v} = \frac{0.01\ \text{mm}}{1250\ \text{mm/s}} = 8x10^{-6}\ \text{s} \qquad (14)$$

where Δt is the step time enable to select for each scanning track. Δx is the smallest element dimension at x- or y- coordinates since the length and width are equal for chosen mesh design with DC3D8. v is scanning speed on powder bed layer. While speed was changing, step time was calculated again and changed.

Before defining other boundary conditions, the room temperature was kept at 25 °C. Convection and radiation were assumed to be from the top surface of the powder bed to the environmental inert gas. Side faces were kept at room temperature T_0, and defined as

$$T(x, y, z, t) = T_0 \qquad (15)$$

At the top surface, heat transfer boundary condition was defined with a temperature dependent k, as;

$$q_{la} = \sigma\varepsilon\left(T^4_{top.} - T^4_{env.}\right) + h_c\left(T - T_{env}\right) + k\left(\frac{\partial^2 T}{x^2} + \frac{\partial^2 T}{y^2} + \frac{\partial^2 T}{z^2}\right) \qquad (16)$$

3. Results and discussion

3.1. Temperature Distribution

Maximum calculated temperature values were plotted in Fig. 5 for different laser power values. For the 1st track, maximum temperatures are between 2850-3000 °C. For the rest of the 3rd scanning track, this interval rises to 3000-3250 °C. Patil and Yadava [43] showed that maximum simulation temperatures are about 2978 K. Kolossov [44] plotted both simulated and experimental temperatures approximately as 2533 and 2400 °C respectively. Both studies were conducted at 2 W power and 1 m/s speed. Romano et al. [45] found the maximum temperatures as 2369.57 K for 100 W with using 100 µm layer thickness. Zhuang et al. [38] predicted maximum temperature approximately as 2500 °C . Huang et al. [35] showed that the maximum temperatures occur among 2400-2600 K in 100 W-120 W interval. Soylemez [46] predicted maximum temperature limit as 3500 °C. On the other hand, maximum temperature changes about 400-600 °C at 2nd or 3rd track from 150 W to 190 W (see Fig. 5). Considering this increment in our simulation, the predicted maximum temperatures can be evaluated coherent with the literature. The effects of hatching distance and scanning speed on temperature results were also presented in Fig. 5. According to the maximal temperatures, heat is transferring from 1st track to the adjacent track faster. Because there is not exist any preheated track or zone at the beginning for 1st track. Heat transfer from 2nd to 3rd or 3rd to 4th track is much smaller and maximum temperatures are much similar to each other. On the other hand, it is seen that the hatch distance is much more important compared to the laser scanning speed. For a linear heat transfer between tracks, among hatch values used in this study, 120 µm can be considered as the most suitable value.

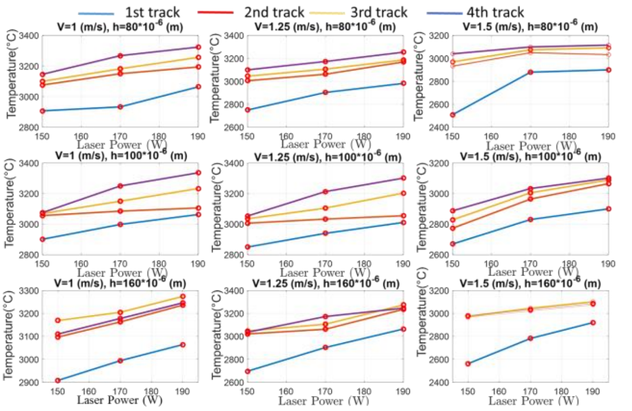

Fig 5. Maximum temperatures against laser power, scanning speed and hatching distance.

3.2. Melt Pool Dimensions

In this study, simulations were conducted with continuously moving laser motion from the beginning to the end of a track. Thus, there is no acceleration effect at the start of tracks. Similarly, at the end of the tracks, laser power cuts off instantaneously which has again an acceleration effect at the end of a track in the manufacturing process. In practice, there are much bigger track zones because of the galvanometer mirror acceleration ramping [47]. In Fig. 6, our simulation results were compared with experimental results in literature [47]. Gong et al. [47] determined the accelerated zone at the beginning of a track approximately as 200 µm. In the simulation, steady melt pool width occurs approximately at 200 µm far away from starting point. Based on this data, melt pools were investigated at a cross-sectional area 300 µm far away from starting point to find melt pool dimensions. For each track, maximum depth (D) and width (W) values were measured and $\frac{D}{W}$ ratios were calculated to determine keyhole possibility. According to the Soylemez, when $\frac{D}{W} > 0.5$, there can be a keyhole problem, and at depth values which satisfies $\frac{D}{W} > 1.2$, keyhole problem is inevitable phenomena [46]. Hence, a critical depth (CD) value was defined to obtain limits of maximum efficient depth values for each track.

When predicted pool depths and widths were compared with the experimental and simulation results in the literature, it was observed that pool dimensions are similar to both experimental and simulation results. Fu and Guo [21] presented the melt pool depths depends on power in interval of approximately 40-120 µm and widths are from 50 to 160 µm levels within error bars in interval of 20 W to 80 W laser power. Romano et al. [45] was predicted melt pool width and depth as 240 and 120 µm for 100 µm layer thickness at 100 W. Soylemez [46] observed width value about 150 µm and depth value about 100 µm for 150 W and 1200 mm/s speed combination. In this study, for 150 W and 1.25 m/s, width and depth were predicted as 143 µm and 54 µm for the 1st track, respectively. Zhuang et al. [38] found depth about 60 µm and width about 180 µm for 120 W power using 30 µm layer thickness at the end of the 5th track. Melt pool depth and width were predicted in the study of Huang et al. [35]. For 120 W power, width and depth were obtained as 150 µm and 60 µm, respectively.

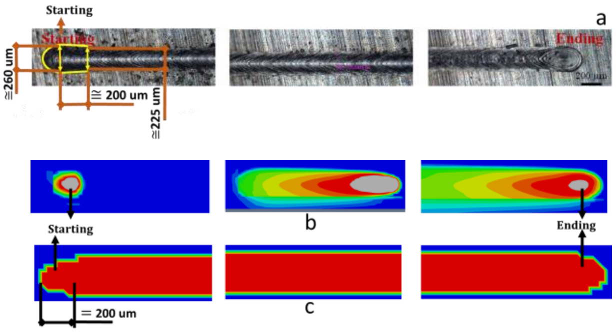

Fig 6. a) Single Laser Track [47], b) Simulation Melt Pool Zone and c) Solidified Zones.

Comparing to the literature, as mentioned above, our melt pool dimensions are similar to the other studies. Discrepancies between simulated melt pool dimensions are probably caused by different laser powers, scanning speeds and hatching distances or assumptions for a low cost simulation.

In Fig. 7, a schematic of simulation melt pool overlaps was shown with different colors to represent the measurement process of pool dimensions. Fig. 7 selected to explain melt pool depth and width calculation process at 190 W- 1.5 m/s – 80 µm. The reason selection of this parameter is that the maximum $\frac{D}{W}$ ratio was at this combination for the 1st track. Calculations done for 27 parameter combinations were given in Table 1.

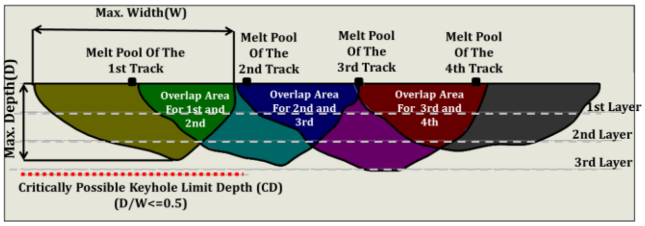

Fig 7. Melt Pool Dimensions For Adjacent 4 Tracks At Cross Section 300 µm Far Away From Initial Point (Parameters; Power=150 W, Speed 1 m/s, Hatch= 120 µm].

With following Fig. 7 for each parameter combination, the biggest $\frac{D}{W}$ ratio was found. Considering tried power, hatch and speed combinations as effective process parameters, thermal model successfully predicted the $\frac{D}{W}$ ratios since there is no keyhole effect was found. On the other hand, it can be seen from Fig. 7 that the overlap area has enough depth to melt all powder since it rises to a depth which about at least two times powder layer thickness.

Table 2 shows CD values for all combinations and at all tracks. It was found that melt pool width and depth predicted as rising and $\frac{\mathrm{D}}{\mathrm{w}}$ ratios as decreasing from 1st track to 4th track regardless of power, speed or hatch distance values. On the other hand, for all combinations, $\frac{\mathrm{D}}{\mathrm{w}}$ ratios were found ≤ 0.5

Table 2. Melt Pool Dimensions, Dimension Ratios and Critical Depth Values For 4 Separate Tracks.

	Speed	Hatch	Power	Depth(D	Width(W	CD	D/W
1st Track	1	80	150	64	164	82	0,39
	1	80	170	69	172	86	0,4
	1	80	190	74	190	95	0,39
	1	100	150	67	172	86	0,39
	1	100	170	69	186	93	0,37
	1	100	190	72	198	99	0,36
	1	120	150	66	165	83	0,4
	1	120	170	74	194	97	0,38
	1	120	190	75	198	99	0,38
	1,25	80	150	54	143	72	0,38
	1,25	80	170	66	162	81	0,41
	1,25	80	190	71	170	85	0,42
	1,25	100	150	58	145	73	0,4
	1,25	100	170	61	162	81	0,38
	1,25	100	190	63	170	85	0,37
	1,25	120	150	57	147	74	0,39
	1,25	120	170	61	154	77	0,4
	1,25	120	190	62	158	79	0,39
	1,5	80	150	50	126	63	0,4
	1,5	80	170	57	144	72	0,4
	1,5	80	190	62	149	75	0,42
	1,5	100	150	51	129	65	0,4
	1,5	100	170	57	143	72	0,4
	1,5	100	190	62	150	75	0,41
	1,5	120	150	55	174	87	0,32
	1,5	120	170	57	181	91	0,31
	1,5	120	190	62	188	94	0,33

	Speed	Hatch	Power	Depth(D	Width(W	CD	D/W
2nd Track	1	80	150	81	204	102	0,4
	1	80	170	93	237	119	0,39
	1	80	190	104	265	133	0,39
	1	100	150	73	206	103	0,35
	1	100	170	86	239	120	0,36
	1	100	190	94	271	136	0,35
	1	120	150	86	224	112	0,38
	1	120	170	90	273	137	0,33
	1	120	190	91	294	147	0,31
	1,25	80	150	84	217	109	0,39
	1,25	80	170	88	230	115	0,38
	1,25	80	190	90	250	125	0,36
	1,25	100	150	68	197	99	0,35
	1,25	100	170	75	224	112	0,33
	1,25	100	190	78	250	125	0,31
	1,25	120	150	72	200	100	0,36
	1,25	120	170	77	218	109	0,35
	1,25	120	190	82	225	113	0,36
	1,5	80	150	78	186	93	0,42
	1,5	80	170	83	211	106	0,39
	1,5	80	190	88	219	110	0,4
	1,5	100	150	58	164	82	0,35
	1,5	100	170	63	205	103	0,31
	1,5	100	190	76	224	112	0,34
	1,5	120	150	72	186	93	0,39
	1,5	120	170	83	223	112	0,37
	1,5	120	190	84	235	118	0,36

	Speed	Hatch	Power	Depth(D	Width(W	CD	D/W
3rd Track	1	80	150	96	267	134	0,36
	1	80	170	102	292	146	0,35
	1	80	190	107	308	154	0,35
	1	100	150	91	281	141	0,32
	1	100	170	104	309	155	0,34
	1	100	190	106	320	160	0,33
	1	120	150	98	290	145	0,34
	1	120	170	100	324	162	0,31
	1	120	190	101	335	168	0,3
	1,25	80	150	94	237	119	0,4
	1,25	80	170	100	255	128	0,39
	1,25	80	190	104	270	135	0,39
	1,25	100	150	73	236	118	0,31
	1,25	100	170	87	285	143	0,31
	1,25	100	190	94	292	146	0,32
	1,25	120	150	85	243	122	0,35
	1,25	120	170	89	272	136	0,33
	1,25	120	190	90	288	144	0,31
	1,5	80	150	88	215	108	0,41
	1,5	80	170	95	236	118	0,4
	1,5	80	190	96	267	134	0,36
	1,5	100	150	65	207	104	0,31
	1,5	100	170	71	249	125	0,29
	1,5	100	190	79	272	136	0,29
	1,5	120	150	82	210	105	0,39
	1,5	120	170	92	248	124	0,37
	1,5	120	190	94	278	139	0,34

	Speed	Hatch	Power	Depth(D	Width(W	CD	D/W
4th Track	1	80	150	108	307	154	0,35
	1	80	170	114	318	159	0,36
	1	80	190	127	367	184	0,35
	1	100	150	91	292	146	0,31
	1	100	170	107	326	163	0,33
	1	100	190	108	341	171	0,32
	1	120	150	106	268	134	0,4
	1	120	170	122	362	181	0,34
	1	120	190	124	382	191	0,32
	1,25	80	150	98	301	151	0,33
	1,25	80	170	111	336	168	0,33
	1,25	80	190	117	352	176	0,33
	1,25	100	150	86	263	132	0,33
	1,25	100	170	91	307	154	0,3
	1,25	100	190	97	340	170	0,29
	1,25	120	150	93	324	162	0,29
	1,25	120	170	101	350	175	0,29
	1,25	120	190	106	370	185	0,29
	1,5	80	150	92	277	139	0,33
	1,5	80	170	101	295	148	0,34
	1,5	80	190	104	311	156	0,33
	1,5	100	150	70	243	122	0,29
	1,5	100	170	76	270	135	0,28
	1,5	100	190	89	302	151	0,29
	1,5	120	150	84	303	152	0,28
	1,5	120	170	86	316	158	0,27
	1,5	120	190	96	340	170	0,28

4. Conclusions

In this study, a detailed 3D finite element heat transfer model for the SLM process was developed based on parameters that were used in EOS M280 SLM device and multi-track simulations were conducted to predict maximum temperatures and melt pool dimensions depends on 27 different process parameter configurations. Results are briefly discussed as follows:

- Predicted maximum temperatures and melt pool dimensions are consistent with existing literature and revealed model gives reliable results.

- According to calculated D/W ratios and CD values, critical keyhole possibility doesn't occur and laser power is more effective than speed and hatch.

- Altough simulation cannot mimic bigger widths at start/end of a track which sourced by the ramping of Galvano mirrors in real manufacturing process, it doesn't cause a problem to predict maximum temperatures or melting pools accurately.

Future study will be on the calibration of the model predictions with the help of experimental multitrack specimen manufacturings. Cross sectional area of EDM machined specimen tracks will be investigated to compare with simulation results. By the way, in-situ temperature measurements by using thermocouple and/or ratio type pyrometer is also planned to provide an experimental data set for maximum temperatures and cooling rates.

Acknowledgments

The authors thankfully acknowledges (TUBİTAK) The Scientific and Technological Research Council of Turkey through Project No: 217M799. Authors also acknowledges SDU-BAP (Suleyman Demirel University-Scientific Research Projects Unity) for their financial support.

Author's statement

Conflict of interest: Authors state no conflict of interest.

References

1. Feygin M. "Apparatus and method for forming an integral object from laminations", US patent 4,752,352, filed April 17th, 1987, published June 1st, 1988.
2. Drstvensek I., Valentan B., Brajlih T., Strojnik T., Ihan H.N., "Direct digital manufacturing as communication and implantation tool in medicine", US-Turkey Workshop On Rapid Technologies, September 24, 2009, 75-81.
3. Hauser, C., Childs, T. H. C., Dalgarno, K. W. "Selective Laser Sintering of Stainless Steel 314S HC Processed Using Room Temperature Powder Beds", Proceedings of the Solid Freeform Fabrication Symposium 1999, University of Texas, Austin, Texas, USA, 273-280.
4. Mercelis P, Kruth J. P.. 2006. "Residual stresses in selective laser sintering and selective laser melting", Rapid Prototyping Journal, 12(5) 254-265.
5. Pohl H., Simchi A., Issa M., Dias H. C., 2001. "Thermal stresses in direct metal laser sintering" Proceedings of the SFF Symposium, 366–372.
6. Agarwala, M., Bourell, D., Beaman, J., Marcus, H. And Barlow, J., 1995. "Direct selective laser sintering of metals", Rapid Prototyping Journal, Vol. 1 No. 1, pp. 26-36.
7. Kellens K., Renaldi R., Dewulf W., Kruth J, Duflou JR. 2014. "Environmental impact modeling of selective laser sintering processes. Rapid Prototyp Journal, 20:459–470. https://doi.org/10.1108/ RPJ-02-2013-0018
8. Khan M., 2010. "Selective laser melting (SLM) of gold (Au)", PhD Thesis, Loughborough University.
9. Matsumoto M., Shiomi M., Osakada K., Abe F., 2002. "Finite element analysis of single layer forming on metallic powder bed in rapid prototyping by selective laser processing", International Journal of Machine Tools and Manufacture, Volume 42, Issue 1, Pages 61-67.
10. Jhabvala J., Boillat E., Antignac T., Glardon R., 2010. "On the effect of scanning strategies in the selective laser melting process". Virtual and Physical Prototyping. 5. 10.1080/17452751003688368.
11. Song B., Dong S., Zhang B., Liao H., Coddet C., 2012. "Effects of processing parameters on microstructure and mechanical property of selective laser melted Ti6Al4V", Materials & Design. 35. 120–125. 10.1016/j.matdes.2011.09.051.
12. Elsayed M., Ghazy M., Youssef Y. and Essa, K., , 2019. "Optimization of SLM process parameters for Ti6Al4V medical implants", Rapid Prototyping Journal, Vol. 25 No. 3, pp. 433-447. https://doi.org/10.1108/RPJ-05-2018-0112
13. Song, B., Dong, S., Liao, H. AND Coddet C., 2012. "Process parameter selection for selective laser melting of Ti6Al4V based on temperature distribution simulation and experimental sintering", Int Journal of Advanced Manufacturing Technology, 61, 967–974. https://doi.org/10.1007/s00170-011-3776-6
14. Zeng K.,. Pal D., Gong H. J., Patil N., Stucker B., 2014. "Comparison of 3DSIM thermal modelling of selective laser melting using new dynamic meshing method to ANSYS", Materials Science and Technology, 31:8, 945-956. DOI: 10.1179/1743284714Y.0000000703.
15. Williams J.D., Deckard C.R., 1998. "Advances in modeling the effects of selected parameters on the SLS process", Rapid Prototyping Journal, Vol. 4 Issue: 2, pp.90-100.
16. Shiomi M.,, Yoshidome A.,, Abe F., Osakada K., 1999. "Finite element analysis of melting and solidifying processes in laser rapid prototyping of metallic powders", International Journal of Machine Tools and Manufacture, Volume 39, Issue 2, , Pages 237-252.
17. Ibraheem A. K., Derby B. , and Withers P. J., 2003. "Thermal and residual stress modelling of the selective laser sintering process", Materials research society symposium proceedings, 47–52; Cambridge, Cambridge University Press.
18. Roberts I. A., C. J. Wang, R. Esterlein, M. Stanford, D. J. Mynors, 2009. "A three-dimensional finite element analysis of the temperature field during laser melting of metal powders in additive layer manufacturing", International Journal of Machine Tools & Manufacture 49, pp916–923.
19. Fischer P., Locher M., Romano V., Weber H.P., Kolossov S., Glardon R., 2003. "Temperature measurements during selective laser sintering of titanium powder", International Journal of "Machine Tools and Manufacture 44(12–13) 1293–1296.
20. Li, R., Shi, Y., Liu, J. Yao H., Zhang W., 2009. "Effects of processing parameters on the temperature field of selective laser melting metal powder" powder metallurgy and metal ceramics, 48: 186. https://doi.org/10.1007/s11106-009-9113-z
21. Fu C., Guo Y.B., 2014. "3-Dimensional finite element modeling of selective laser melting Ti-6Al-4V alloy",

Conference: 25th Annual International Solid Freeform Fabrication Symposium, August 2014 , Austin, Texas.

22. Lindgren L. E., Lundbäck A., Fisk M., Pederson R., Andersson J, 2016. “Simulation of additive manufacturing using coupled constitutive and microstructure models”, Additive Manufacturing 12 , 144–158.
23. Luo Z.,, Zhao Y., 2019. “Efficient thermal finite element modeling of selective laser melting of Inconel 718”, Computational Mechanics 65(Supplement C):1-25 .
24. Zeng K., Pal D., Stucker B., 2012. “A review of thermal analysis methods in laser sintering and selective laser melting”, Proceedings of Solid Freeform Fabrication Symposium Austin, TX 60, 796-814.
25. Lavery N., P., Brown S.G.R., Sienz J., Cherry J., Belblidia F., 2014. “A review of computational modelling of additive layer, manufacturing - multi-scale and multi-physics” , International Conference on Sustainable Design and Manufacturing Cardiff, Wales, UK 28-30 April 2014.
26. Schoinochoritis B., Chantzis D., Salonitis K., 2017. “Simulation of metallic powder bed additive manufacturing processes with the finite element method: A critical review”, Proceedings of the Institution of Mechanical Engineers, Part B: Journal of Engineering Manufacture, ; 231(1):96-117. doi:10.1177/0954405414567522
27. Hajializadeh F., Ince A., 2019. “Finite element–based numerical modeling framework for additive manufacturing process”, Special Issue Article, Volume-1, Issue1, February 2019, e28.
28. Moraes D. A. and Czekanski A., 2018. “Parametric thermal FE analysis on the laser power input and powder effective thermal conductivity during selective laser melting of SS304L”, Journal of Manufacturing and Materials Processing 2(3): 47.
29. Parry L., Ashcroft I. A., Wildman R., 2016. “Understanding the effect of laser scan strategy on residual stress in selective laser melting through thermo-mechanical simulation” , Additive Manufacturing Volume 12, Part A, October 2016, Pages 1-15.
30. Bejan, A., & Kraus, A. D. 2003. “Heat transfer handbook”, New York: J. Wiley.
31. Goldak J., Chakravarti A. and Bibby M., 1984. “A new finite element model for welding heat sources”, Metallurgical Transactions B volume 15, pages 299–305.
32. Denlinger, E.R., Irwin, J., and Michaleris, P., 2014. “Thermomechanical modeling of additive manufacturing large parts”, Journal of Manufacturing Science and Engineering, 136(6), 061007.
33. Hocine S., Swygenhoven H. V., Petegem S. V., 2021. “Verification of selective laser melting heat source models with operando X-ray diffraction data”, Additive Manufacturing 37 (2021) 101747.
34. Zhang Q., Xie J., Gao Z., London T., Griffiths D., Oancea V., 2019. “A metallurgical phase transformation framework applied to SLM additive manufacturing processes”, Materials & Design Volume 166, 15 March 2019, 107618.
35. Huang Y., Yang L. J., Du X.Z., Yang Y.P., 2016. “Finite element analysis of thermal behavior of metal powder during selective laser melting”, International Journal of Thermal Sciences 104 146 e 157.
36. Dai K., Shaw L., 2005. “Finite element analysis of the effect of volume shrinkage during laser densification”, Acta Materialia 53 , 4743–4754
37. Mills KC., 2002. “Recommended values of thermophysical properties for selected commercial Alloys”, Wiltshire, England; Woodhead.
38. Zhuang J. R., Wen T. L., An H. H., Yang S., 2018. “Determination of melt pool dimensions using DOE-FEM and RSM with process window during SLM of Ti6Al4V powder”, Optics and Laser Technology 103, 59–76.
39. Teng C., Ashby K., Phan N, Pal D., Stucker B., 2016. “The effects of material property assumptions on predicted meltpool shape for laser powder bed fusion based additive manufacturing”, Measurement Science and Technology, 27, 085602 (8pp).
40. Teng, C., Gong H., Szabo A., Dilip J.j.s., Ashby K., Zhang S., Patil N., Pal D., Stucker Bren. 2017. “Simulating melt pool shape and lack of fusion porosity for selective laser melting of cobalt chromium components”, Journal of Manufacturing Science and Engineering. 139. 10.1115/1.4034137
41. Zhao X., Iyer A., Promoppatum P., Yao S. C., 2017. “Numerical modeling of the thermal behavior and residual stress in thedirect metal laser sintering process of titanium alloy products”, Additive Manufacturing, Volume 14, March 2017, Pages 126-136.
42. Arısoy Y. M., Criales L., Ozel T., 2019. “Modeling and simulation of thermal field and solidification in laser powder bed fusion of nickel alloy IN625”, Optics & Laser Technology 109:278-292.
43. Patil B., Yadava V., 2007. “Finite element analysis of temperature distribution in single metallic powder layer during metal laser sintering”, International Journal of Machine Tools & Manufacture 47, 1069–1080.
44. Kolossov S., Boillat E., Glardon R., Fischer P., Locher M., 2004 . “3D FE simulation for temperature evolution in the selective laser sintering process”, International Journal of Machine Tools & Manufacture 44 117–123.
45. Romano J., Ladani L., Sadowski M., 2015.” Thermal modeling of laser based additive manufacturing processes within common materials”, Procedia Manufacturing, Volume 1, Pages 238-250.
46. Soylemez E., 2019. “Modeling the melt pool of the laser sintered Ti6Al4V layers with goldak’s double-ellipsoidal heat source”, Solid Freeform Fabrication 2018: Proceedings of the 29th Annual International Solid Freeform Fabrication Symposium – An Additive Manufacturing Conference.
47. Gong H., Gu H., Zeng K., Dilip J.J.S., Pal D., Stucker B., 2014. “Melt pool characterization for selective laser melting of Ti-6Al-4V pre-alloyed powder”